

# Entangled photon pair generation from an epsilon-near-zero metasurface

Wenhe Jia<sup>1,2,#</sup>, Grégoire Saerens<sup>2,#</sup>, Ülle-Linda Talts<sup>2</sup>, Helena Weigand<sup>2</sup>, Robert J. Chapman<sup>2</sup>, Liu Li<sup>1</sup>, Rachel Grange<sup>2,\*</sup>, Yuanmu Yang<sup>1,\*</sup>

<sup>1</sup>State Key Laboratory for Precision Measurement Technology and Instruments, Department of Precision Instrument, Tsinghua University, Beijing 100084, China

<sup>2</sup>Optical Nanomaterial Group, Institute for Quantum Electronics, Department of Physics, ETH Zurich, Zurich 8093, Switzerland

#These authors contributed equally to this work.

\*Corresponding authors: [granger@ethz.ch](mailto:granger@ethz.ch) or [ymyang@tsinghua.edu.cn](mailto:ymyang@tsinghua.edu.cn)

**Entangled photon pair sources are essential for diverse quantum technologies, such as quantum communication, computation, and imaging. Currently, most methods for generating and manipulating entangled photon pairs rely on bulk nonlinear crystals, with some requiring sophisticated engineering. In this work, we propose and experimentally demonstrate a 68-nm-thick entangled photon pair source using a plasmonic metasurface strongly coupled to an epsilon-near-zero (ENZ) material. By tailoring dual resonances at both pump and emission wavelengths and utilizing the field enhancement induced by the ENZ effect, the photon pair generation efficiency is boosted. The coincidences-to-accidentals ratio of the generated photon pairs reaches 40, well above the limit of classical light radiation. Moreover, the ENZ metasurface platform enables versatile manipulation of the system's anisotropic second-order nonlinear susceptibility tensor, allowing for direct control over the polarization states of the generated photon pairs. By conducting polarization-resolved second-harmonic generation measurements, we discuss the potential to achieve a polarization-entangled Bell state from the identical ENZ metasurface, based on the quantum-classical correspondence. Our approach opens a new avenue for simultaneously achieving the miniaturization of photon pair sources and quantum state engineering.**

**Keywords:** photon pair generation, spontaneous parametric down-conversion, epsilon-near-zero, metasurface

## 1. Introduction

Entangled photon pair source is a fundamental component of modern quantum technologies, such as quantum communication<sup>1</sup>, computation<sup>2</sup>, imaging<sup>3</sup>, and sensing<sup>4</sup>. One of the most common methods for generating entangled photon pairs is via the spontaneous parametric down-conversion (SPDC) process in birefringent crystals with a nonvanishing second-order nonlinear optical susceptibility<sup>5</sup>. Through coherent superposition of different SPDC processes<sup>6</sup> or post-selection methods<sup>7</sup>, diverse entangled quantum states can be generated. However, these methods need to strictly satisfy the phase-matching conditions, which typically require additional manufacturing steps such as periodic poling or engineered birefringence<sup>6-8</sup>.

Recently, metasurfaces composed of sub-wavelength geometry antennas have drawn significant attention in the development of compact entangled photon pair sources<sup>9-13</sup>. They enable the relaxation of phase-matching conditions and support resonances at pump or emission wavelengths to effectively

boost the efficiency of the SPDC processes<sup>14</sup>. Moreover, metasurfaces offer flexibility in the simultaneous multi-dimensional manipulation of the generated photon pairs. By customizing for specific wavelength<sup>15</sup>, emission angle<sup>16, 17</sup>, direction<sup>18</sup>, and polarization<sup>19</sup>, metasurfaces facilitate the generation of complex entangled states at sub-wavelength scales. Particularly, plasmonic metasurfaces provide a versatile platform for engineering the anisotropic nonlinear susceptibility tensors of materials<sup>20, 21</sup>, which holds the potential to tune the polarization states of the generated photon pairs. This may further enable the generation of polarization-entangled quantum states.

While plasmonic metasurfaces have been widely applied for manipulating various nonlinear processes<sup>21-23</sup>, the experimental demonstration of the photon pair generation from plasmonic metasurfaces has not yet been achieved and only theoretically proposed<sup>24, 25</sup>. The smaller mode volume and higher ohmic losses of plasmonic metasurfaces compared to their dielectric counterparts may result in a lower nonlinear conversion efficiency<sup>20</sup>, which impedes their use in the SPDC process.

One solution to enhance the nonlinearity of plasmonic metasurfaces is to strongly couple them with an epsilon-near-zero (ENZ) material. In recent years, ENZ materials, with the real part of the permittivity approaching zero<sup>26</sup>, have been widely used in nonlinear optics<sup>27-29</sup>. The low group velocity of light near its ENZ wavelengths leads to a significant electric field amplification<sup>30</sup>, which has been utilized to enhance various nonlinear frequency conversion processes<sup>31-33</sup>. Furthermore, it has been demonstrated that ENZ material can significantly boost the nonlinear response of plasmonic metasurfaces by constructing strongly coupled systems<sup>34-36</sup>.

In this work, we experimentally demonstrate the photon pair generation via the SPDC process from a 68-nm-thick ENZ metasurface composed of indium tin oxide (ITO) thin film and gold (Au) plasmonic resonators, as schematically illustrated in Fig. 1. By strongly coupling to an ENZ material and tailoring resonances at both the pump and emission wavelengths, the generation efficiency of photon pairs is boosted, and a normalized efficiency of 0.08 Hz/mW/ $\mu\text{m}$  is achieved. The coincidences-to-accidentals ratio (CAR) of the generated photon pairs is 40, well above the limit for classical light radiation. Moreover, we manipulate the polarization states of photon pairs by designing the anisotropic second-order nonlinear susceptibility tensor of the ENZ metasurface. We further investigate the potential for generating a polarization-entangled Bell state<sup>37</sup> from one identical ENZ metasurface, as indicated by the polarization-resolved second-harmonic generation (SHG) measurements, based on the quantum-classical correspondence<sup>37-40</sup>.

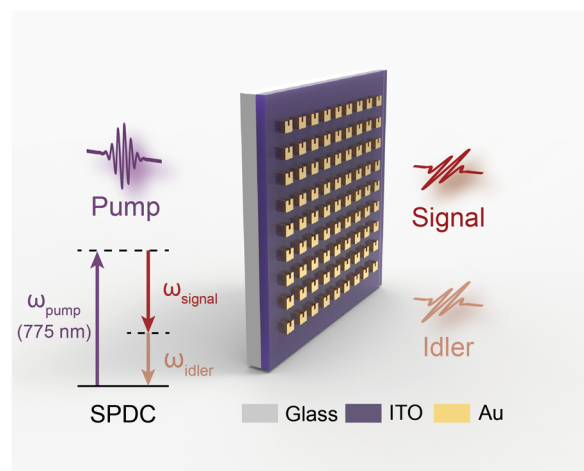


**Figure 1** | Schematic illustration of entangled photon pair generation from an ultrathin plasmonic

metasurface composed of gold (Au) split-ring resonators (SRRs) via the spontaneous parametric down-conversion (SPDC) process. By strongly coupling to an epsilon-near-zero (ENZ) material indium tin oxide (ITO) thin film, the generation efficiency of the photon pair can be significantly enhanced. The metasurface exhibits resonances near both the pump (775 nm) and the signal/idler (near 1550 nm) wavelengths to boost the SPDC process.

## 2. Results

### ENZ Metasurface design and characterization

To enhance the photon pair generation efficiency of the plasmonic metasurface, we strongly couple it with an ENZ material. A commercially available ENZ material, a 23-nm-thick indium tin oxide (ITO) thin film on a float glass substrate (PGO GmbH), is utilized to support the plasmonic metasurfaces composed of gold split-ring resonators (SRRs). The dispersion curve of its permittivity is measured via spectroscopic ellipsometry, revealing the real part of its permittivity crossing zero at 1420 nm (see Section 1 in the Supplementary Information for details about the linear characteristics of the ITO film).

The geometric parameters of the SRR are swept to find parameters that experimentally support a magnetic dipole resonance near the ENZ wavelength of the underlying ITO film<sup>22</sup>. This design establishes a strongly coupled system and engineers a resonance close to both the signal and idler wavelengths near 1550 nm, which is expected to greatly enhance the nonlinear response of the plasmonic metasurfaces<sup>35</sup>. The simulated transmission spectra as a function of the ITO film's ENZ wavelength show the anti-crossing shape resonances near 1200 nm and 1600 nm (Fig. 2a), indicating a strong coupling effect between the SRRs and the ENZ film<sup>34</sup>. Meanwhile, an electric dipole resonance is supported at the pump wavelength of 775 nm<sup>22</sup>, achieving a dual enhancement in the photon pair generation. Compared to dielectric metasurfaces, the resonances and the associated field enhancements in a plasmonic metasurface can be relatively broadband, which makes it more tolerant to fabrication errors. The geometric parameters of the SRRs are illustrated in Fig. 2b. The nanostructure array with a size of  $200 \times 200 \mu\text{m}^2$  is fabricated via a single-step electron beam lithography and lift-off process, with a scanning electron microscope (SEM) image displayed in Fig. 2c.

The transmittance spectra are measured for two orthogonal polarizations, referred to as x- and y-polarization, as depicted in Fig. 2d, respectively. The experimental results are in good agreement with the simulations, revealing resonances near both the pump and the signal/idler wavelengths. Since gold<sup>41</sup> and ITO<sup>31, 42</sup> possess surface second-order nonlinearity, the photon pair generation is expected to originate from the gold-ITO interface. To estimate the field confinement and the related SPDC enhancement, we simulated the electric field amplitude distribution at this position. As depicted on the right side of Fig. 2d, the electric field amplitude is significantly amplified by over two orders of magnitude as a result of the strong coupling effect, which can be utilized to enhance the photon pair generation efficiency.

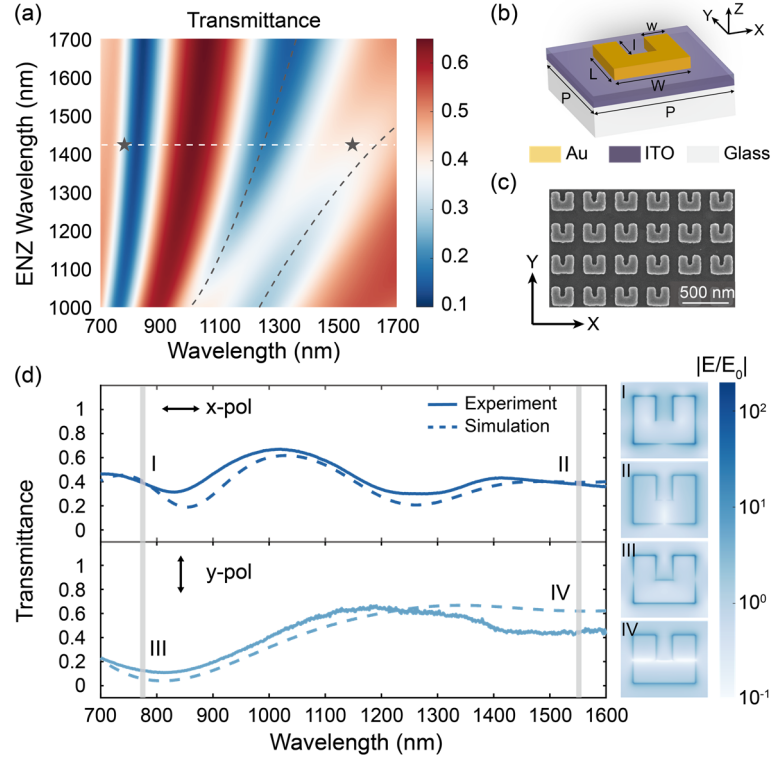


**Figure 2 | ENZ Metasurface design and characterization.** (a) Simulated linear transmittance spectra of the strongly coupled metasurface under x-polarized light as a function of ITO film's ENZ wavelength. The dashed lines indicate the measured ENZ wavelength (white) and the anti-crossing shape resonances (grey). The stars mark the pump (775 nm) and signal/idler (near 1550 nm) wavelengths in the following SPDC measurements. (b) Schematic of a gold split-ring resonator (SRR) coupled to an ITO film. The geometric parameters are as follows:  $P = 350$  nm,  $W = 248$  nm,  $L = 217$  nm,  $w = 89$  nm, and  $l = 112$  nm. The ITO layer is 23-nm-thick and the gold layer is 40-nm-thick. A 5-nm-thick titanium layer is used as the adhesion layer. (c) The scanning electron microscope (SEM) image of the fabricated ENZ metasurface. (d) Measured (solid) and simulated (dashed) transmittance spectra of the ENZ metasurface for x- (upper panel) and y- (lower panel) polarized light, respectively. The grey markers indicate the pump (775 nm) and the signal/idler (near 1550 nm) wavelengths in the following SPDC measurements. The electric field amplitude distributions (normalized to the incident field) at the gold-ITO interface (x-y plane) are shown on the right side.

### Photon pair generation measurements

To characterize the photon pairs generated from the ENZ metasurface, we built a Hanbury-Brown-Twiss (HBT) setup, as schematically shown in Fig. 3a and also described in our previous works<sup>40, 43</sup>. A continuous-wave (CW) laser with a wavelength of 775 nm is focused using a high numerical aperture lens ( $NA = 0.5$ ) to pump the ENZ metasurface. The full width at half maximum (FWHM) of the spot's diameter is approximately 5  $\mu\text{m}$ . The generated photon pairs are collected by an identical lens and then separated from the pump laser using two long-pass filters and a band-pass filter. After being coupled into a fiber, the photon pairs pass through a 50:50 fiber beam splitter and are detected by two isolated superconducting nanowire single-photon detectors (SNSPDs). A time-to-digital converter (TDC) is utilized to obtain the coincidence histogram from two channels (see Methods for details about the experimental setup).



Figure 3b displays the measured coincidence histogram from the ENZ metasurface with an integration time of 2 hours and a pump power of 3 mW, showing a clear peak at zero time delay. To further confirm the non-classical nature of the generated photon pairs, we calculate the second-order correlation function  $g^{(2)}(t)$ , as shown in the inset of Fig. 3b. The corresponding CAR =  $g^{(2)}(0)-1$  is 40, well above the classical photon radiation limit of 2. The emission rate normalized to the thickness and pump power is 0.08 Hz/mW/ $\mu\text{m}$ , which is comparable with the recently investigated LiNbO<sub>3</sub> metasurface-based photon pair emitters<sup>14, 16, 44</sup>. The generation efficiency comparison to other compact photon pair sources is discussed in Section 3 in the Supplementary Information.

To further investigate the mechanism of the photon pair generation, we measure the power dependence of the coincident counts, as shown in Fig. 3c. The coincident counts exhibit a linear relationship with the pump power, and  $g^{(2)}(0)$  is inversely proportional to the pump power, aligning with the scaling law of the SPDC process<sup>45</sup> (see Section 2 in the Supplementary Information for details about  $g^{(2)}(0)$  characterization).

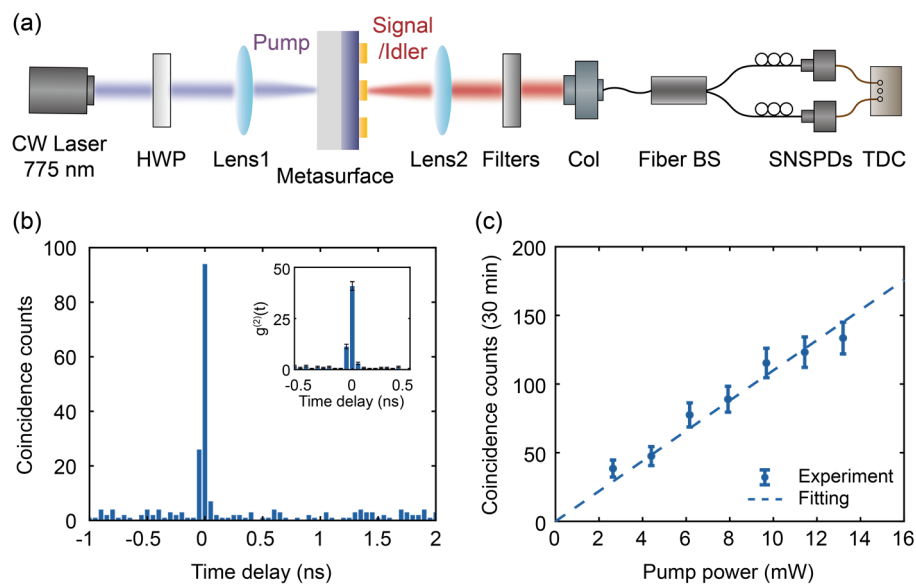


**Figure 3| Photon pair generation and characterization.** (a) Schematic illustration of the Hanbury-Brown-Twiss (HBT) setup. HWP, half-wave plate; Col, fiber collimator; BS, beam splitter; SNSPDs, superconducting nanowire single-photon detectors; TDC, time-to-digital converter. (b) Measured coincidence histogram from the ENZ metasurface with an integration time of 2 hours and a pump power of 3 mW. Inset: the second-order correlation function  $g^{(2)}(t)$  showing a coincidences-to-accidentals ratio (CAR) of 40. (c) Measured coincidence counts from the ENZ metasurface (dots) and the corresponding linear fitting curve (line) as a function of the pump power.

### Polarization characterization of photon pairs

The nonlinear response of the SRR nanostructures originates from the breaking of structural symmetry<sup>22</sup>. SHG measurements could be utilized to characterize the nonlinear response of materials. When excited by x-polarized light, the magnetic dipole resonance can induce a continuous nonlinear current around the SRR, resulting in the generation of coherent second-order nonlinear polarization along its two bars<sup>22, 46</sup>. This process facilitates the orthogonally polarized type-1 SHG, as schematically depicted in the upper panel of Fig. 4a. It can be represented by  $|HH\rangle_{s,i} \rightarrow |V\rangle_p$ , where we denote x- and y-polarization

as  $H$  and  $V$ , respectively. However, under  $y$ -polarized pumping, the nonlinear polarization induced from two bars of SRR interferes destructively in the far field, preventing the generation of the second-harmonic wave<sup>22, 46</sup>. The nonlinear response of the metasurface can be described using the effective second-order nonlinear susceptibility tensor<sup>47</sup>, which is inferred as follows<sup>48</sup>:  $\chi_{xxx}^{(2)} = 0$ ,  $\chi_{yyy}^{(2)} = 0$ ,  $\chi_{xyy}^{(2)} = 0$ , and  $\chi_{yxx}^{(2)} \neq 0$ . Moreover, based on the Kleinman symmetry condition<sup>48</sup>, we can further derive other elements:  $\chi_{xyy}^{(2)} = \chi_{yyx}^{(2)} = \chi_{yxy}^{(2)} = 0$ , and  $\chi_{yxx}^{(2)} = \chi_{xxy}^{(2)} = \chi_{xyx}^{(2)} \neq 0$ .

To further confirm that the nonlinear response of the SRRs follows the derived effective second-order nonlinear susceptibility tensor, we measure the polarization states of the second-harmonic wave under various pump configurations (see Methods for details about the experimental setup). Figure 4b depicts the SHG intensity as a function of the pump and detection polarization angles. When pumped with  $x$ -polarized light, a  $y$ -polarized SHG is observed, while no SHG is detected under  $y$ -polarized light excitation. Our measurements align well with the theoretical calculations based on the effective nonlinear susceptibility tensor, as shown in Section 4 in the Supplementary Information.

The quantum-classical correspondence links the efficiency of SPDC with that of its inverse processes, such as sum-frequency generation (SFG) or SHG, indicating the polarization dependency of both the excitation and frequency-converted photons<sup>37-40</sup>. Consequently, the polarization states of both the signal and idler photons can be estimated using the effective second-order nonlinear susceptibility tensor as well. For instance, when pumped with  $y$ -polarized light, both the signal and idler photons are expected to be  $x$ -polarized following the type-1 SPDC process, as schematically depicted in the middle panel of Fig. 4a, which can be represented as  $|V\rangle_p \xrightarrow{\chi_{yxx}^{(2)}} |HH\rangle_{s,i}$ .

To further characterize the polarization states of the photon pairs, a linear polarizer is set before the fiber collimator. We measure the coincident counts as a function of the detection polarization angle when pumped with  $y$ -polarized light, as shown in Fig. 4c. The coincidence counts reach a maximum when the polarizer is set to  $x$ -polarized ( $\theta = 0^\circ$ ), while the photon pairs are nearly absent with  $y$ -polarized ( $\theta = \pm 90^\circ$ ) detection. This result is in agreement with the theoretical detection angle dependence  $N \propto T(\theta)^2 = \cos^4\theta$ , where  $T(\theta)$  is the transmittance of  $x$ -polarized light through the polarizer, and  $\theta$  is the transmissive angle of the polarizer with respect to the  $x$ -axis. This finding further confirms the quantum-classical correspondence between SHG and SPDC in terms of polarization.

Furthermore, when pumped with  $x$ -polarized light, the generated signal and idler photons are expected to exhibit orthogonal linear polarizations, as schematically illustrated in the bottom panel of

Fig. 4a. This type-2 SPDC process occurs through two pathways:  $|H\rangle_p \xrightarrow{\chi_{xxy}^{(2)}} |HV\rangle_{s,i}$  and  $|H\rangle_p \xrightarrow{\chi_{xyx}^{(2)}} |VH\rangle_{s,i}$ , each with equal probabilities. The resulting state is a coherent superposition of states from these two pathways, represented as  $|H\rangle_p \rightarrow \frac{1}{\sqrt{2}}(|HV\rangle_{s,i} + |VH\rangle_{s,i})$ , indicating the generation of a Bell state from the identical ENZ metasurface.

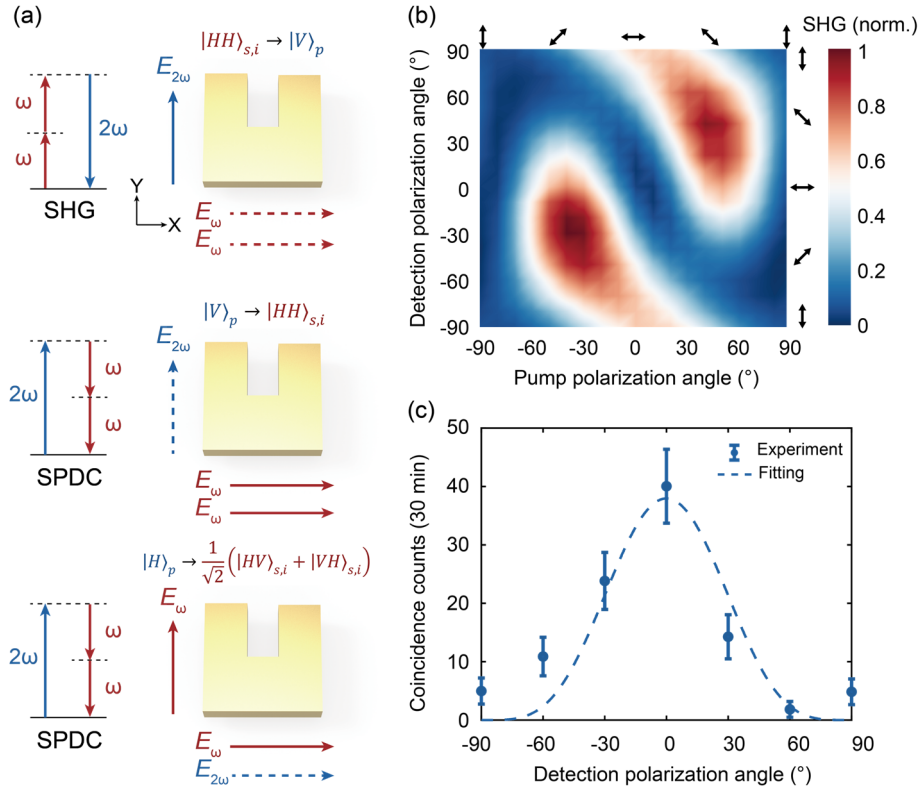


**Figure 4 | Polarization characterization of the photon pairs generated from the ENZ metasurface.** (a) Schematic illustration of the polarization characteristics of the second-harmonic generation (SHG) process (upper panel) and the SPDC processes with different pump configurations (middle and bottom panels). (b) Measured SHG intensity from the ENZ metasurface as a function of the pump and the detection polarization angles. Both the pump and detection polarization states are linearly polarized, as indicated by the arrows. (c) Measured coincidence counts from the ENZ metasurface under y-polarized pumping (dots) and the fitting curve (line) as a function of the detection polarization angle. The coincidence counts fit with the function,  $N \propto \cos^4 \theta$ , where  $\theta$  is the transmissive angle of the polarizer with respect to the x-axis. At  $\theta = 0^\circ$ , detection is performed with x-polarization, while at  $\theta = \pm 90^\circ$ , detection is performed with y-polarization.

### 3. Conclusion

To summarize, we experimentally demonstrate photon pair generation via the SPDC process from a 68-nm-thick plasmonic metasurface strongly coupled to an ENZ material. By tailoring resonances at both the pump and emission wavelengths and leveraging the field enhancement induced by the ENZ effect, we achieve a normalized photon pair generation efficiency of 0.08 Hz/mW/ $\mu\text{m}$ , which is comparable with the recently investigated LiNbO<sub>3</sub> metasurface-based photon pair emitters. The CAR of the photon pairs is 40, significantly exceeding the limit of classical light radiation. Furthermore, the polarization states of the generated photon pairs are controlled by designing the system's anisotropic nonlinear susceptibility tensor. We lastly discuss the potential of generating a polarization-entangled Bell state using the identical ENZ metasurface through polarization-resolved SHG measurements.

In the future, we could utilize resonances with higher quality factors such as quasi-bound states in the continuum resonance<sup>49</sup> or surface lattice resonance<sup>50</sup> to achieve greater field enhancement. Alternatively, integrating metasurfaces with resonant cavities could enable multiple interactions between pump light and metasurfaces<sup>51</sup>, to further boost the photon pair generation efficiency. Moreover,

ENZ metasurfaces hold the potential for manipulating the polarization state of the photon pairs by controlling their rotational symmetry and the pumping polarization, enabling the generation of tunable polarization-entangled photon pair sources<sup>37, 52</sup>. Furthermore, by engineering the orientation and geometric parameters of the unit cells, the phase difference between signal and idler photons may be controlled flexibly, thus facilitating the generation of hyper-entanglement states<sup>53</sup>. Our work shows the potential of achieving miniaturized and multifunctional entangled photon pair sources using ENZ metasurfaces, which provides a platform for developing compact quantum devices capable of generating and manipulating quantum states simultaneously.

## Methods

**Photon pair generation measurements.** A continuous-wave laser at a wavelength of 775 nm (Toptica DL pro780) is used as the pump light, which is focused onto the metasurface through a high-NA lens (Thorlabs A240TM,  $f = 8$  mm,  $NA = 0.5$ ). The polarization angle of the pump light can be tuned using a half-wave plate (HWP). The photon pairs generated from the ENZ metasurface are collected and collimated using an identical lens. Two long-pass filters (Semrock LP1064 and LP1319) and a band-pass filter with a central wavelength of 1550 nm and a bandwidth of 50 nm (Edmund Optics BP1550) are used to block the pump light. The photon pairs are then coupled into the single-mode fiber through a fiber collimator (Thorlabs CFC11A-C,  $f = 11$  mm). A linear polarizer is set before the collimator to characterize the polarization states of the photon pairs. After passing through a 50:50 beam splitter, the photon pairs are detected by two isolated superconducting nanowire single-photon detectors (SNSPDs). Finally, we could obtain the coincidence histogram through the time-digital converter (TDC). Since the SNSPDs are sensitive to a specific linear polarization state, we first calibrate the setup using a laser with a wavelength of 1550 nm and tunable polarization states. Two fiber polarization controllers are utilized to maximize the photon detection efficiencies of the SNSPDs.

**SHG measurements** A Ti: sapphire laser is employed to pump an optical parametric oscillator (Coherent Chameleon OPO) for generating femtosecond laser pulses with a wavelength of 1550 nm, a pulse duration of 200 fs, and a repetition rate of 80 MHz. A high-NA lens (Thorlabs A240TM,  $f = 8$  mm,  $NA = 0.5$ ) is employed to focus the laser onto the ENZ metasurface, resulting in a spot diameter with an FWHM of approximately 5  $\mu\text{m}$ . The generated second-harmonic wave is collected by a 100 $\times$  objective (Olympus LMPlanFLN,  $NA = 0.8$ ) and detected by a visible-range CMOS camera (Andor Zyla sCMOS). The pump beam is filtered using two short-pass filters (Thorlabs FESH0900). The pump power is set to 0.5 mW, and an HWP is utilized to control the pump polarization states. A linear polarizer is employed for characterizing the SHG polarization state.

## Data availability

All relevant data are available in the main text, Supporting Information, or from the authors.

## Acknowledgment

The authors thank Dr. Shuai Wang for the insightful discussion. This work was supported by the National Natural Science Foundation of China (Grants 62135008 and 61975251), the Swiss National Science Foundation SNSF (Consolidator Grants 2022 213713, and 179099) as well as the European Union's Horizon 2020 research and innovation program from the European Research Council under the Grant Agreement No. 714837 (Chi2-nanooxides). H.W. acknowledges financial support from the

Physics Department at ETH Zurich. R.J.C. acknowledges support from the Swiss National Science Foundation under the Ambizione Fellowship Program (Project Number 208707).

### Author contributions

Y.Y., R.G., and W.J. conceived this work. W.J. designed the metasurface. W.J., G.S. U.T., and H.W. characterized the ITO film and metasurface. G.S. built the SPDC measurement setup. W.J. conducted the experiments. W.J., G.S., R.J.C., and L.L. analyzed the data. W.J., G.S., Y.Y., and R.G. wrote the manuscript. All the authors discussed the results. Y.Y. and R.G. supervised the project.

### Competing interests

The authors declare no competing interests.

### References

1. Saglamyurek E., *et al.* Broadband waveguide quantum memory for entangled photons. *Nature* **469**, 512-515 (2011).
2. O'Brien J. L. Optical quantum computing. *Science* **318**, 1567-1570 (2007).
3. Lemos G. B., Borish V., Cole G. D., Ramelow S., Lapkiewicz R., Zeilinger A. Quantum imaging with undetected photons. *Nature* **512**, 409-412 (2014).
4. Pirandola S., Bardhan B. R., Gehring T., Weedbrook C., Lloyd S. Advances in photonic quantum sensing. *Nat. Photonics* **12**, 724-733 (2018).
5. Harris S. E., Oshman M. K., Byer R. L. Observation of Tunable Optical Parametric Fluorescence. *Phys. Rev. Lett.* **18**, 732-734 (1967).
6. Kim T., Fiorentino M., Wong F. N. C. Phase-stable source of polarization-entangled photons using a polarization Sagnac interferometer. *Phys. Rev. A* **73**, 012316 (2006).
7. Anwar A., Perumangatt C., Steinlechner F., Jennewein T., Ling A. Entangled photon-pair sources based on three-wave mixing in bulk crystals. *Rev. Sci. Instrum.* **92**, 041101 (2021).
8. Bouchard F., *et al.* Two-photon interference: the Hong-Ou-Mandel effect. *Rep. Prog. Phys.* **84**, 012402 (2021).
9. Solntsev A. S., Agarwal G. S., Kivshar Y. S. Metasurfaces for quantum photonics. *Nat. Photonics* **15**, 327-336 (2021).
10. Liu J., Shi M., Chen Z., Wang S., Wang Z., Zhu S. Quantum photonics based on metasurfaces. *Opto-Electron. Adv.* **4**, 200092 (2021).
11. Wang K., Chekhova M., Kivshar Y. Metasurfaces for quantum technologies. *Phys. Today* **75**, 38-44 (2022).
12. Sharapova P. R., Kruk S. S., Solntsev A. S. Nonlinear Dielectric Nanoresonators and Metasurfaces: Toward Efficient Generation of Entangled Photons. *Laser Photonics Rev.* **17**, 2200408 (2023).
13. Ma J., *et al.* Engineering Quantum Light Sources with Flat Optics. *Adv. Mater.*, e2313589 (2024).
14. Santiago-Cruz T., *et al.* Photon Pairs from Resonant Metasurfaces. *Nano Lett.* **21**, 4423-4429 (2021).
15. Santiago-Cruz T., *et al.* Resonant metasurfaces for generating complex quantum states. *Science* **377**, 991-995 (2022).
16. Zhang J., *et al.* Spatially entangled photon pairs from lithium niobate nonlocal metasurfaces. *Sci. Adv.* **8**, eabq4240 (2022).
17. Weissflog M. A., *et al.* Directionally Tunable Co- and Counter-Propagating Photon Pairs from a Nonlinear Metasurface. *ArXiv*: 2403.07651 (2024).

18. Son C., *et al.* Photon pairs bi-directionally emitted from a resonant metasurface. *Nanoscale* **15**, 2567-2572 (2023).
19. Ma J., *et al.* Polarization Engineering of Entangled Photons from a Lithium Niobate Nonlinear Metasurface. *Nano Lett.* **23**, 8091-8098 (2023).
20. Kauranen M., Zayats A. V. Nonlinear plasmonics. *Nat. Photonics* **6**, 737-748 (2012).
21. Li G., Zhang S., Zentgraf T. Nonlinear photonic metasurfaces. *Nat. Rev. Mater.* **2**, 1-14 (2017).
22. Klein M. W., Enkrich C., Wegener M., Linden S. Second-harmonic generation from magnetic metamaterials. *Science* **313**, 502-504 (2006).
23. Krasnok A., Tymchenko M., Alu A. Nonlinear metasurfaces: a paradigm shift in nonlinear optics. *Mater. Today* **21**, 8-21 (2018).
24. Ming Y., *et al.* Photonic Entanglement Based on Nonlinear Metamaterials. *Laser Photonics Rev.* **14**, 1900146 (2020).
25. Jin B. Y., Mishra D., Argyropoulos C. Efficient single-photon pair generation by spontaneous parametric down-conversion in nonlinear plasmonic metasurfaces. *Nanoscale* **13**, 19903-19914 (2021).
26. Alam M. Z., De Leon I., Boyd R. W. Large optical nonlinearity of indium tin oxide in its epsilon-near-zero region. *Science* **352**, 795-797 (2016).
27. Liberal I., Engheta N. Near-zero refractive index photonics. *Nat. Photonics* **11**, 149-158 (2017).
28. Reshef O., De Leon I., Alam M. Z., Boyd R. W. Nonlinear optical effects in epsilon-near-zero media. *Nat. Rev. Mater.* **4**, 535-551 (2019).
29. Kinsey N., DeVault C., Boltasseva A., Shalaev V. M. Near-zero-index materials for photonics. *Nat. Rev. Mater.* **4**, 742-760 (2019).
30. Khurgin J. B., *et al.* Adiabatic frequency shifting in epsilon-near-zero materials: the role of group velocity. *Optica* **7**, 226-231 (2020).
31. Capretti A., Wang Y., Engheta N., Dal Negro L. Comparative Study of Second-Harmonic Generation from Epsilon-Near-Zero Indium Tin Oxide and Titanium Nitride Nanolayers Excited in the Near-Infrared Spectral Range. *ACS Photonics* **2**, 1584-1591 (2015).
32. Yang Y., *et al.* High-harmonic generation from an epsilon-near-zero material. *Nat. Phys.* **15**, 1022-1026 (2019).
33. Jia W., *et al.* Broadband terahertz wave generation from an epsilon-near-zero material. *Light Sci. Appl.* **10**, 11 (2021).
34. Alam M. Z., Schulz S. A., Upham J., De Leon I., Boyd R. W. Large optical nonlinearity of nanoantennas coupled to an epsilon-near-zero material. *Nat. Photonics* **12**, 79-83 (2018).
35. Deng J., Tang Y., Chen S., Li K., Zayats A. V., Li G. Giant Enhancement of Second-Order Nonlinearity of Epsilon-near-Zero Medium by a Plasmonic Metasurface. *Nano Lett.* **20**, 5421-5427 (2020).
36. Jia W., *et al.* Intracavity spatiotemporal metasurfaces. *Adv. Photonics* **5**, 026002 (2023).
37. Weissflog M. A., *et al.* A Tunable Transition Metal Dichalcogenide Entangled Photon-Pair Source. *ArXiv*: 2311.1603 (2023).
38. Marino G., *et al.* Spontaneous photon-pair generation from a dielectric nanoantenna. *Optica* **6**, 1416-1422 (2019).
39. Kulkarni G., Rioux J., Braverman B., Chekhova M. V., Boyd R. W. Classical model of spontaneous parametric down-conversion. *Phys. Rev. Research* **4**, 033098 (2022).
40. Saerens G., *et al.* Background-Free Near-Infrared Biphoton Emission from Single GaAs Nanowires. *Nano Lett.* **23**, 3245-3250 (2023).
41. Wang F. X., Rodríguez F. J., Albers W. M., Ahorinta R., Sipe J. E., Kauranen M. Surface and bulk

- contributions to the second-order nonlinear optical response of a gold film. *Phys. Rev. B* **80**, 233402 (2009).
42. Rodriguez-Sune L., *et al.* Study of second and third harmonic generation from an indium tin oxide nanolayer: Influence of nonlocal effects and hot electrons. *APL Photonics* **5**, 010801 (2020).
  43. Hanh Duong N. M., *et al.* Spontaneous parametric down-conversion in bottom-up grown lithium niobate microcubes. *Opt. Mater. Express* **12**, 3696-3704 (2022).
  44. Fedotova A., *et al.* Lithium Niobate Meta-Optics. *ACS Photonics* **9**, 3745-3763 (2022).
  45. Ivanova O. A., Iskhakov T. S., Penin A. N., Chekhova M. V. Multiphoton correlations in parametric down-conversion and their measurement in the pulsed regime. *Quantum Electron.* **36**, 951-956 (2006).
  46. Ciraci C., Poutrina E., Scalora M., Smith D. R. Origin of second-harmonic generation enhancement in optical split-ring resonators. *Phys. Rev. B* **85**, 201403 (2012).
  47. Lee J., *et al.* Giant nonlinear response from plasmonic metasurfaces coupled to intersubband transitions. *Nature* **511**, 65-69 (2014).
  48. Boyd R. W. *Nonlinear Optics*. Academic Press (2020).
  49. Liang Y., *et al.* Bound States in the Continuum in Anisotropic Plasmonic Metasurfaces. *Nano Lett.* **20**, 6351-6356 (2020).
  50. Bin-Alam M. S., *et al.* Ultra-high-Q resonances in plasmonic metasurfaces. *Nat. Commun.* **12**, 974 (2021).
  51. Mekhael M., *et al.* Phase-Matched Second-Harmonic Generation from Metasurfaces Inside Multipass Cells. *ACS Photonics* **11**, 682-687 (2024).
  52. Wu Y., *et al.* Optical spin-orbit interaction in spontaneous parametric downconversion. *Optica* **10**, 538-543 (2023).
  53. Graffitti F., *et al.* Hyperentanglement in structured quantum light. *Phys. Rev. Research* **2**, 043350 (2020).



## Supplementary Information:

### Entangled photon pair generation from an epsilon-near-zero metasurface

Wenhe Jia<sup>1,2,#</sup>, Grégoire Saerens<sup>2,#</sup>, Ülle-Linda Talts<sup>2</sup>, Helena Weigand<sup>2</sup>, Robert J. Chapman<sup>2</sup>, Liu Li<sup>1</sup>, Rachel Grange<sup>2,\*</sup>, Yuanmu Yang<sup>1,\*</sup>

<sup>1</sup>State Key Laboratory for Precision Measurement Technology and Instruments, Department of Precision Instrument, Tsinghua University, Beijing 100084, China

<sup>2</sup>Optical Nanomaterial Group, Institute for Quantum Electronics, Department of Physics, ETH Zurich, Zurich 8093, Switzerland

#These authors contributed equally to this work.

\*Corresponding authors: [granger@ethz.ch](mailto:granger@ethz.ch) or [ymyang@tsinghua.edu.cn](mailto:ymyang@tsinghua.edu.cn)

#### 1. Linear characteristics of ITO film

A commercially available ITO film on a float glass substrate (PGO GmbH) is utilized to construct the strongly coupled system with the plasmonic nanostructures. The dispersion curve of ITO film's permittivity is measured via spectroscopic ellipsometry, as shown in Fig. S1, and it follows the Drude model<sup>1</sup>:

$$\varepsilon_{\text{ITO}}(\omega) = \varepsilon_{\infty} - \frac{\omega_p^2}{\omega^2 + i\gamma\omega} \quad (\text{S1})$$

where  $\omega$  is the optical frequency,  $\varepsilon_{\infty} = 4.42$  is the permittivity at high frequency,  $\omega_p = 2.84 \times 10^{15}$  rad/s is the plasma frequency, and  $\gamma = 2.58 \times 10^{14}$  rad/s is the damping frequency. The real part of its permittivity crosses zero at the wavelength of 1420 nm.

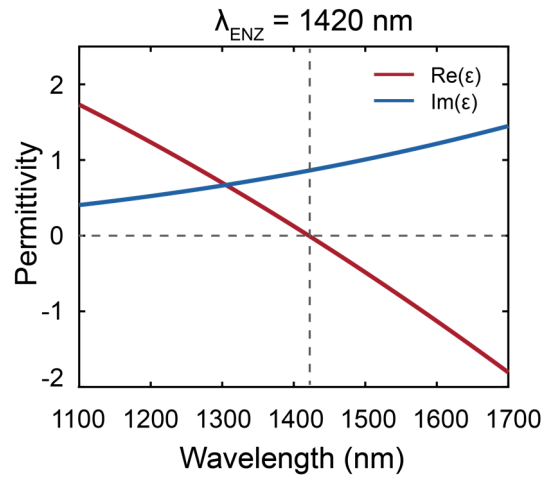


**Figure S1** | Real (red) and imaginary (blue) parts of the permittivity of the ITO film. The ENZ wavelength appears at 1420 nm, marked with the grey dashed line.

#### 2. $g^{(2)}(0)$ characterization of the generated photon pairs

To further confirm the non-classical nature of the photon pairs generated from the ENZ metasurface, we calculate the second-order correlation function at zero time delay  $g^{(2)}(0)$  following the equation<sup>2</sup>:

$$g^{(2)}(0) = \frac{R_c}{R_s R_i T_c} \quad (\text{S2})$$

where  $R_c$  is the rate of coincidence counts,  $R_s$  and  $R_i$  are the rates of signal and idler photon counts, respectively, and  $T_c$  is the time resolution of the coincidence histogram. As  $R_c$ ,  $R_s$ , and  $R_i$  exhibit linear dependence of the pump power,  $g^{(2)}(0)$  is inversely proportional to the pump power. Our measurements align with the theoretical power dependence, as depicted in Fig. S2.

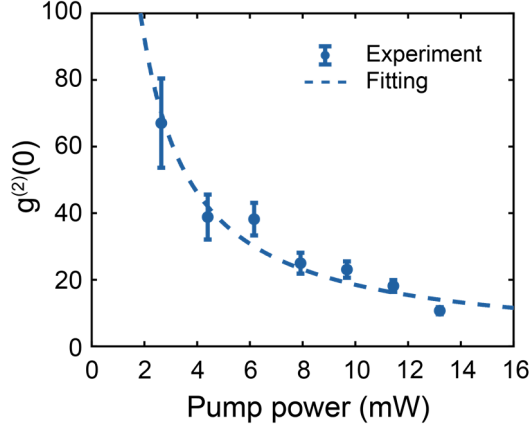


**Figure S2**| Measured second-order correlation function at zero time delay  $g^{(2)}(0)$  (dots) and the corresponding fitted curve (line) as a function of the pump power, indicating an inversely proportional relationship.

### 3. Generation efficiency comparison with other metasurface-based compact photon pair sources

To compare the generation efficiency of various compact photon pair sources, for which the SPDC was also obtained in different conditions, the emission rate is normalized by the thickness and pump power<sup>3</sup>. The normalized efficiency of the ENZ metasurface is 0.08 Hz/mW/ $\mu$ m, which is comparable with the recently investigated LiNbO<sub>3</sub>, GaAs, and GaP metasurface-based photon pair emitters, as summarized in Table S1.

Platform	Thickness ( $\mu$ m)	Power (mW)	Photon pair rate (Hz/mW/ $\mu$ m)
LiNbO <sub>3</sub> metasurface <sup>4</sup>	0.68	70	0.11
LiNbO <sub>3</sub> + silica metagrating <sup>5</sup>	0.504	85	0.04
LiNbO <sub>3</sub> + multiplexed silica metagratings <sup>6</sup>	0.515	85	0.02
GaAs metasurface <sup>7</sup>	0.505	9.6	0.02
GaP metasurface <sup>8</sup>	0.15	20	0.02
ENZ metasurface (our work)	0.068	3	0.08

**Table S1**| Comparison of metasurface-based compact photon pair sources.

### 4. Theoretical SHG polarization dependence of the ENZ metasurface

The nonlinear response of the ENZ metasurface can be described using the effective second-order nonlinear susceptibility tensor as follows<sup>9, 10</sup>:  $\chi_{xxx}^{(2)} = 0$ ,  $\chi_{yyy}^{(2)} = 0$ ,  $\chi_{xyy}^{(2)} = \chi_{yyx}^{(2)} = \chi_{yxy}^{(2)} = 0$ , and

$\chi_{yxx}^{(2)} = \chi_{xxy}^{(2)} = \chi_{xyx}^{(2)} \neq 0$ . With this description, we analyze the polarization state of the second-

harmonic wave under different pump configurations. The x and y components of the generated SHG are calculated using the equations,

$$E_x^{2\omega} = \chi_{xxy}^{(2)} E_x^\omega E_y^\omega + \chi_{xyx}^{(2)} E_y^\omega E_x^\omega \quad (\text{S2})$$

$$E_y^{2\omega} = \chi_{yxx}^{(2)} E_x^\omega E_x^\omega \quad (\text{S3})$$

where  $E_x^\omega = E_0^\omega \cos\alpha$  and  $E_y^\omega = E_0^\omega \sin\alpha$  are the x and y components of the pump light,  $\alpha$  is the polarization angle of the pump light with respect to the x-axis, and  $E_0$  is the amplitude of the pump light.

The electric field component with an angle  $\theta$  to the x-axis of second-harmonic wave is calculated following the equation,

$$E_\theta^{2\omega} = E_x^{2\omega} \cos\theta + E_y^{2\omega} \sin\theta \quad (\text{S4})$$

To compare the theoretical calculations with the measurements, we calculate the SHG intensity as a function of the pump and detection angles following  $I_\theta^{2\omega} \propto |E_\theta^{2\omega}|^2$ , as shown Fig. S3. The consistency between theoretical results and measurements (Fig. 4b in the main text) confirms that the nonlinear response of the ENZ metasurface adheres to the derived effective second-order nonlinear susceptibility tensor.

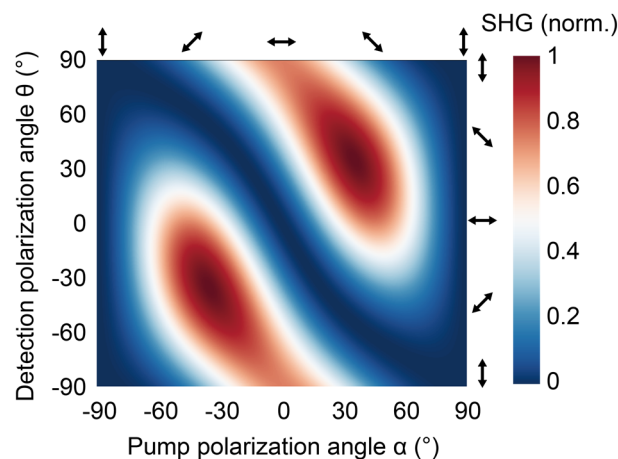


**Figure S3**| Calculated SHG intensity from the ENZ metasurface as a function of the pump and the detection polarization angles based on the derived effective second-order nonlinear susceptibility tensor. Both the pump and detection polarization states are linearly polarized, as indicated by the arrows.

## References

1. Alam M. Z., De Leon I., Boyd R. W. Large optical nonlinearity of indium tin oxide in its epsilon-near-zero region. *Science* **352**, 795-797 (2016).
2. Okoth C., Cavanna A., Santiago-Cruz T., Chekhova M. V. Microscale Generation of Entangled Photons without Momentum Conservation. *Phys. Rev. Lett.* **123**, 263602 (2019).
3. Fedotova A., *et al.* Lithium Niobate Meta-Optics. *ACS Photonics* **9**, 3745-3763 (2022).
4. Santiago-Cruz T., *et al.* Photon Pairs from Resonant Metasurfaces. *Nano Lett.* **21**, 4423-4429 (2021).
5. Zhang J., *et al.* Spatially entangled photon pairs from lithium niobate nonlocal metasurfaces. *Sci. Adv.* **8**, eabq4240 (2022).
6. Ma J., *et al.* Polarization Engineering of Entangled Photons from a Lithium Niobate Nonlinear Metasurface. *Nano Lett.* **23**, 8091-8098 (2023).

7. Santiago-Cruz T., *et al.* Resonant metasurfaces for generating complex quantum states. *Science* **377**, 991-995 (2022).
8. Son C., *et al.* Photon pairs bi-directionally emitted from a resonant metasurface. *Nanoscale* **15**, 2567-2572 (2023).
9. Boyd R. W. *Nonlinear Optics*. Academic Press (2020).
10. Lee J., *et al.* Giant nonlinear response from plasmonic metasurfaces coupled to intersubband transitions. *Nature* **511**, 65-69 (2014).